Supporting Information

$K_8Ce_2I_{18}O_{53}$: A New Potassium Cerium (IV) Iodate with Enhanced Visible-Light Driven Photocatalytic Activity Resulting from Zero Dimensional $[Ce(IO_3)_8]^{4-}$ Unit

Ruofei Wu,[a,b] Xingxing Jiang,[a] Mingjun Xia,[*,a] Lijuan Liu,[a] Xiaoyang Wang,[a] Zheshuai Lin,[a] and Chuangtian Chen[a]

[a]Beijing Center for Crystal Research and Development, Key Laboratory of Functional Crystals and Laser Technology, Technical Institute of Physics and Chemistry, Chinese Academy of Sciences, Beijing 100190, China.

[b]University of Chinese Academy of Sciences, Beijing 100049, China.

Contents：

1. Powder X-ray diffraction

2. Single crystal structure determination

3. Element analysis

4. IR spectrum

5. Thermal analysis

6. UV-VIS-NIR diffuse reflectance spectrum

7. Tables

Table S1. Crystal data and structure refinement for $K_8Ce_2I_{18}O_{53}$.

Table S2. Selected bond lengths (Å) and angles (degree) for $K_8Ce_2I_{18}O_{53}$.

Table S3. Positional coordinates and equivalent isotropic displacement parameters for $K_8Ce_2I_{18}O_{53}$

8. Figures

Figure S1. Experimental (red) and simulated (black) X–ray powder diffraction patterns of $K_8Ce_2I_{18}O_{53}$.

Figure S2. XPS measurement on $K_8Ce_2I_{18}O_{53}$.

Figure S3. Elemental analysis of $K_8Ce_2I_{18}O_{53}$.

Figure S4. IR spectra of $K_8Ce_2I_{18}O_{53}$.

Figure S5. Thermal gravimetric (TG) and differential scanning calorimetry (DSC) analysis of $K_8Ce_2I_{18}O_{53}$.

Figure S6. Experimental (red) and simulated (black) X–ray powder diffraction patterns of residues after TG analysis.

Figure S7. UV-vis-NIR diffuse reflectance spectra of $K_8Ce_2I_{18}O_{53}$.

Figure S8. Different mechanism of RhB degradation in $K_8Ce_2I_{18}O_{53}$ and P25.

.

1. Powder X-ray diffraction: Powder X-ray powder diffraction analysis in the range $2\theta = 10-70°$with a 0.02° scan step width and a 0.05s / step counting time was performed with the use of an automated Bruker D8 X-ray diffractometer equipped with Cu $K\alpha$ radiation (λ= 1.5418 Å). The results were compared with simulated ones derived from single crystal structure.

2. **XPS measurement:** The X-ray photoelectron spectroscopy (XPS) experiments were carried out by a Thermo Scientific Escalab 250Xi system equipped with a monochromatic Al-$K\alpha$ X-ray source. The spectra were registered after purging the samples at ambient temperature under vacuum (residual pressure < 10^{-7} Pa). An electron flood gun compensated the sample charging during the measurement. The electron take off angle was 45° with respect to the sample surface, and the analyzer was operated in constant pass energy mode (46.95 eV). The C_{1s} signal at 284.8 eV was used as an internal standard for calibration of the XPS-signals.

2. Single crystal structure determination: A $K_8Ce_2I_{18}O_{53}$ crystal with the dimensions of 0.12 × 0.10 × 0.09 mm^3 was chosen for single crystal X-ray diffraction measurement. The crystal data were collected by using graphite-monochromated Mo $K\alpha$ radiation (λ = 0.71073Å) on a Bruker APEX II single crystal X-ray diffractometer at 153 K. The structure was solved with direct method by program SHELXS-97 and refined by the full matrix least squares on F^2 by SHELXL-97, respectively. All atoms were refined with anisotropic displacement parameters. The crystal structure was verified by the ADDSYM algorithm using program PLATON and no additional symmetry was given.

3. Element Analysis: Elemental analysis of the crystals was performed on an EDX-equipped Hitachi S-4800 SEM instrument, and the results showed that the crystals consisted of I : Ce : K in a molar ratio of 9 : 1.06 : 3.83 which is consistent with the theoretical ratio (9 : 1 : 4).

4. IR spectrum: Infrared (IR) spectrum was measured at room temperature with a Bio-Rad FTS-60 FTIR spectrometer in the range 400-4000 cm^{-1} with a resolution of 1 cm^{-1}. The sample was mixed thoroughly with dried KBr at a mass ratio of 1:100.

5. Thermal analysis: The thermal gravimetric analysis (TGA) was performed with a

NETZSCH STA 409C/CD thermal analyzer. In detail, an 18.8 mg powder sample was thoroughly ground, carefully placed in a platinum crucible, and heated from room temperature to 1050 °C at a rate of 10 °C/min in a flowing nitrogen atmosphere. $K_8Ce_2I_{18}O_{53}$ shows high stability in thermal analysis, it is stable up to 400 °C and displays three main steps of weight loss, which are in 412-505 °C, 505-600 °C, and 660-918 °C, respectively. The final residue are confirmed as CeO_2 which account for 7.24% of total mass, whereas the calculated number is 9.2%.

6. UV-vis-NIR diffuse reflectance spectrum: The diffuse reflectance spectrum of $K_8Ce_2I_{18}O_{53}$ was measured on a Varian Cary 5000 UV−vis−NIR spectrophotometer with a $BaSO_4$ plate used as a reference material (100% reflectance). The optical absorption spectra were converted from diffuse reflectance spectra using the Kubelka−Munk function, $F(R) = \alpha/S = (1-R)^2/2R$, where R is the diffuse reflectance and α and S are the Kubelka−Munk absorption and scattering coefficients, respectively. The results shows $K_8Ce_2I_{18}O_{53}$ has a high transmission in the range from 500 nm – 2.5 μm.

Table S1. Crystal data and structure refinement for $K_8Ce_2I_{18}O_{53}$.

Empirical formula	$K_8Ce_2I_{18}O_{53}$
Formula weight	3725.24
Temperature	153.15
Wavelength (Å)	0.71073
Crystal system	Monoclinic
Space group	*C2/c*
a(Å)	18.2793(7)
b(Å)	11.4855(7)
c(Å)	13.2212(6)
β(°)	100.471(2)
Volume(^{3})e	2709.5(2)
Z	2
Density (g cm^{-3})	4.533
μ (mm^{-1})	12.564
F(000)	3292
GOF on F^2	1.063
R indices [$I>2\sigma(I)$][a]	$R_1 = 0.0437$, $wR_2 = 0.1151$
R indices [all data][a]	$R_1 = 0.0485$, $wR_2 = 0.1177$

[a] $R_1 = \sum \| \| F_o \| - \| F_c \| \| / \sum | F_o |$;.w$R_2 = \{(\sum [w(F_o^2 - F_c^2)^2] / \sum wF_o^4 \}^{1/2}$

Table S2. Selected bond lengths (Å) and angles (degree) for $K_8Ce_2I_{18}O_{53}$.

Ce(1)-O(8)	2.270(8)	Ce(1)-O(3)	2.325(8)
Ce(1)-O(5)	2.361(8)	Ce(1)-O(11)	2.385(8)
I(1)-O(4)	1.822(3)	I(1)-O(2)	1.868(1)
I(1)-O(4)#2	1.822(3)	I(1)-O(2) #2	1.868(1)
I(2)-O(7)	1.789(1)	I(2)-O(12)	1.802(9)
I(2)-O(5)	1.846(8)	I(3)-O(9)	1.783(1)
I(3)-O(13)	1.812(9)	I(3)-O(8)	1.855(8)
I(4)-O(6)	1.788(9)	I(4)-O(10)	1.807(9)
I(4)-O(3)	1.834(8)	I(5)-O(1)	1.905(1)
I(5)-O(14)	1.781(1)	I(5)-O(11)	1.834(8)
K(1)-O(1)	2.491(1)	K(1)-O(3)	2.655(9)
K(1)-O(6)	2.699(9)	K(1)-O(10)	2.828(1)
K(1)-O(7)	2.839(1)	K(1)-O(12)	2.896(1)
K(1)-O(4)	3.09(3)	K(1)-O(5)	3.140(9)
K(2)-O(9)	2.654(1)	K(2)-O(6)	2.848(1)
K(2)-O(2)	2.857(1)	K(2)-O(12)	2.882(1)
K(2)-O(9)	2.908(1)	K(2)-O(7)	2.957(1)
K(2)-O(14)	3.386(2)	K(2)-O(10)	3.045(1)
O(9)#1-Ce(1)-O(9)	97.7(4)	O(9)-Ce(1)-O(12)#5	66.8(2)
O(9)#1-Ce(1)-O(5)#2	132.3(2)	O(5)#2-Ce(1)-O(12)#5	137.0(3)
O(9)-Ce(1)-O(5)#2	77.5(3)	O(5)#3-Ce(1)-O(12)#5	65.9(2)

Table S3. Coordinates, equivalent isotropic displacement parameters and bond valence sums (BVS) for $K_8Ce_2I_{18}O_{53}$.

Atom	x/a	y/b	z/c	Ueq [Å^2]	BVS
Ce1	0.0000	0.13442(8)	0.7500	0.0099(2)	4.15
I1	0.0000	0.62121(12)	0.7500	0.0379(4)	4.69
I2	0.92919(4)	0.88098(6)	0.55381(6)	0.0179(2)	5.03
I3	0.12950(4)	0.36539(6)	0.65479(6)	0.0161(2)	4.97
I4	0.70529(4)	0.60777(6)	0.84771(5)	0.0127(2)	5.05
I5	0.91652(5)	0.64287(8)	0.04191(7)	0.0265(3)	4.66
K1	0.84788(2)	0.8731(3)	0.8381(2)	0.0333(7)	1.40
K2	0.78623(1)	0.6240(3)	0.6081(2)	0.0308(7)	1.01
O1	0.9409(8)	0.7349(12)	0.9328(11)	0.065(4)	
O2	0.9247(9)	0.5173(14)	0.6947(12)	0.073(4)	
O3	0.6205(4)	0.5649(7)	0.7590(6)	0.0175(17)	
O4	0.9699(1)	0.684(3)	0.862(2)	0.015(7)	
O5	0.9943(4)	0.9904(8)	0.6214(6)	0.0204(19)	
O6	0.7326(5)	0.7274(8)	0.7764(7)	0.025(2)	
O7	0.9024(6)	0.8048(8)	0.6588(7)	0.032(2)	
O8	0.0497(4)	0.2649(7)	0.6526(6)	0.0211(18)	
O9	0.1667(6)	0.2931(10)	0.5564(7)	0.041(3)	
O10	0.7609(5)	0.4963(8)	0.8012(7)	0.028(2)	
O11	0.9091(5)	0.7692(8)	0.1250(7)	0.026(2)	
O12	0.8490(5)	0.9704(8)	0.5106(7)	0.0251(19)	
O13	0.0727(6)	0.4755(10)	0.5816(11)	0.062(4)	
O14	0.8188(6)	0.6319(11)	0.9973(9)	0.052(3)	

Figure S1. Experimental (red) and simulated (black) X–ray powder diffraction patterns of $K_8Ce_2I_{18}O_{53}$.

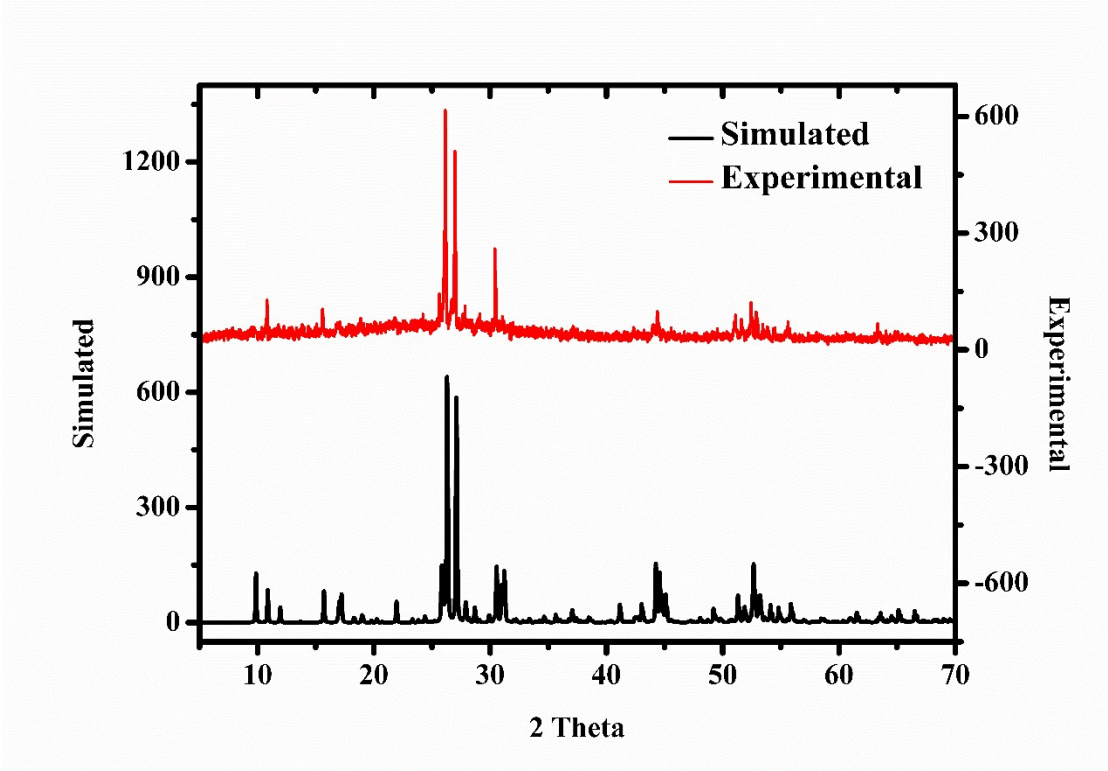

Figure S2. XPS measurement on $K_8Ce_2I_{18}O_{53}$.

The binding energy (BE) at 917.0 ±0.2 eV (Peak 6) associated to the Ce $3d_{3/2}$ is characteristic of the presence of tetravalent Ce (Ce^{4+} ions) in Ce-compounds, and also known as fingerprint of Ce (IV) compounds. In comparison with the Ce 3d XPS spectra collected in previous reports, the shape of the $3d_{5/2}$ and $3d_{3/2}$ spin-orbit peaks reveal the presence of contributions at about 880.2, 884.3 and 899.8, 903.3±0.2 eV. All these six peaks are attributed to the pairs of spin-orbit doublets in Ce (IV) states.

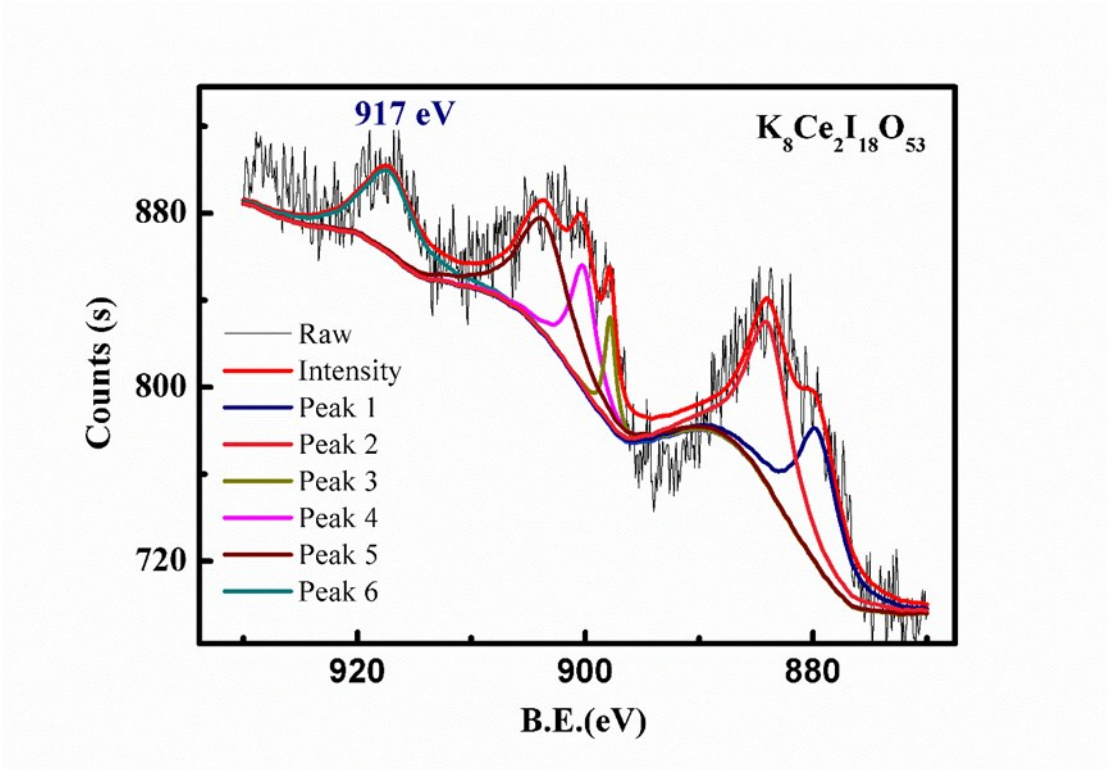

Figure S3. Element analysis of $K_8Ce_2I_{18}O_{53}$.

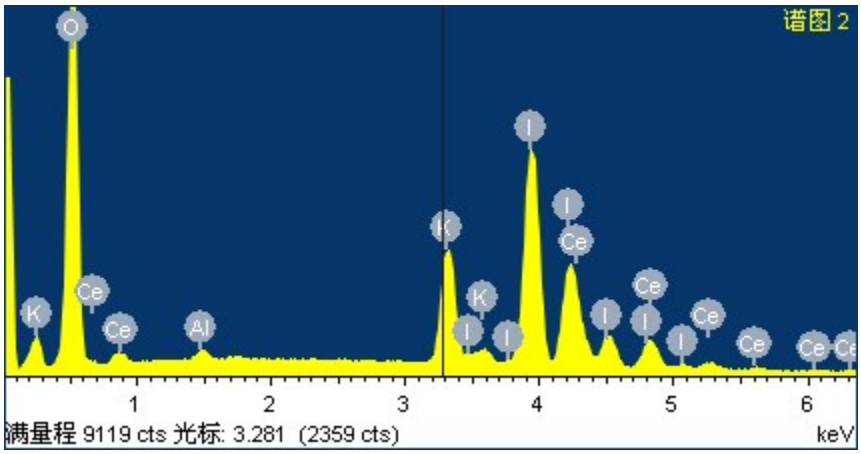

Element	Mass (%)	Molar (%)
O K	30.52	73.36
Al K	0.49	0.70
K K	7.70	7.58
I L	54.24	16.43
Ce L	7.04	1.93
Total	100.00	100.00

Figure S4. IR spectra of $K_8Ce_2I_{18}O_{53}$.

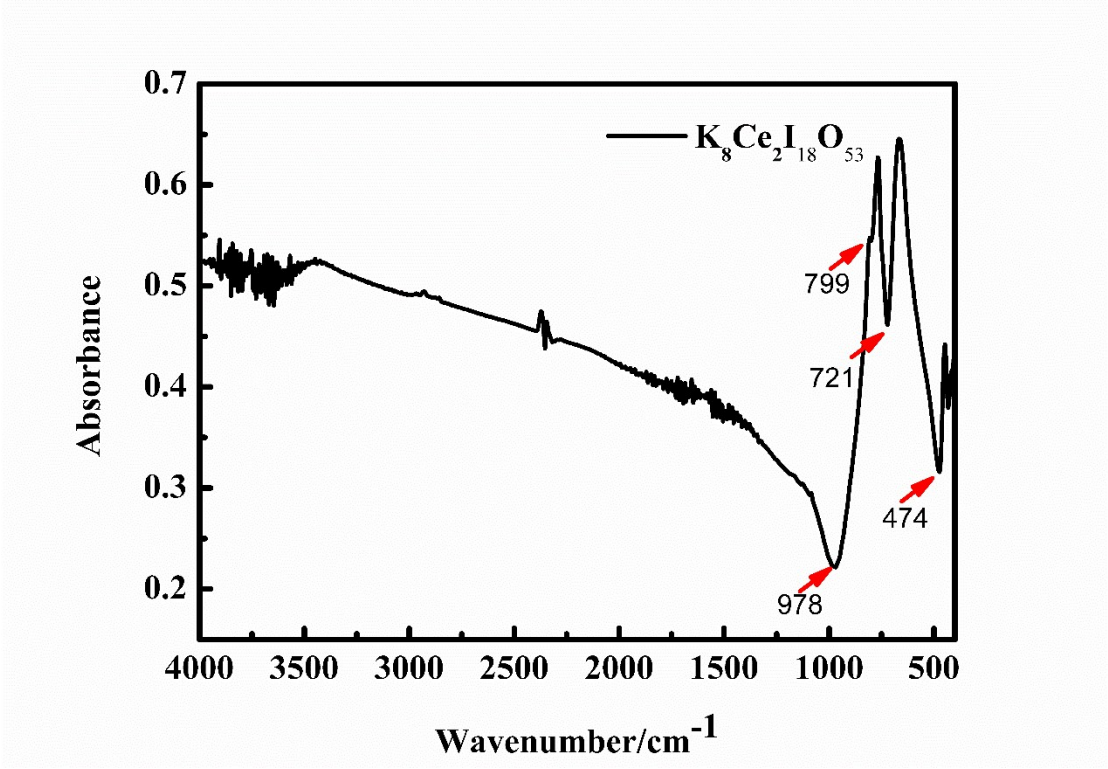

Figure S5. Thermal gravimetric (TG) and differential scanning calorimetry (DSC) analysis of $K_8Ce_2I_{18}O_{53}$.

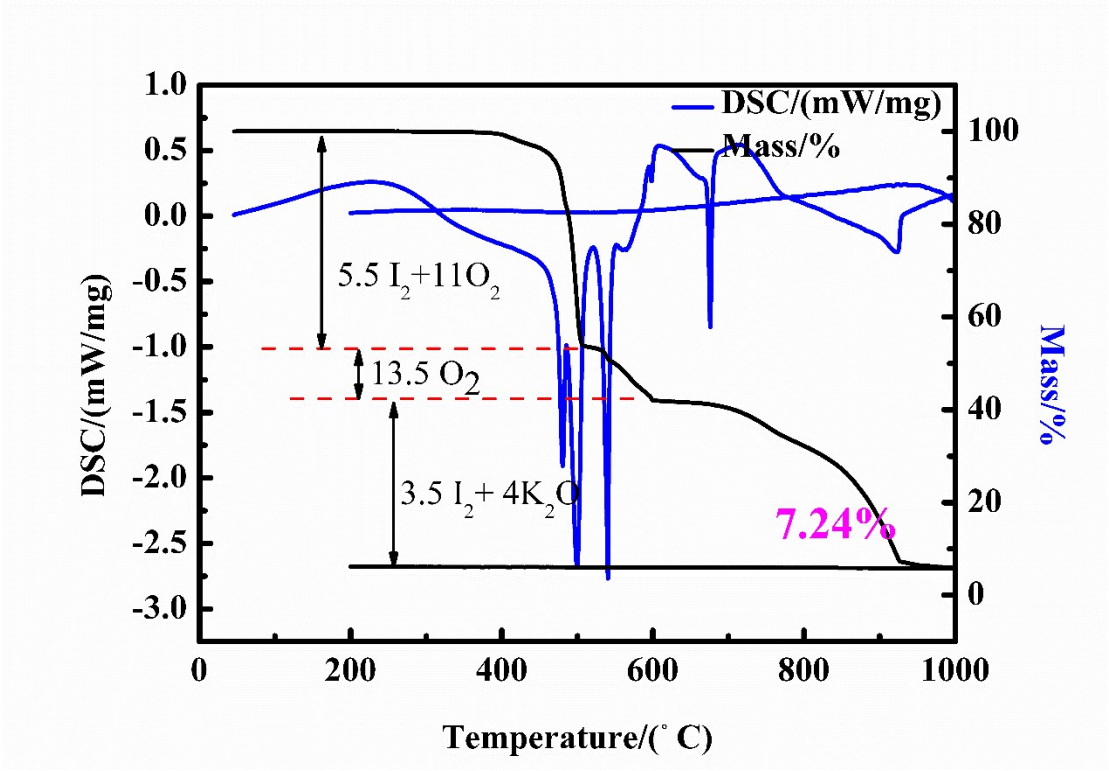

Figure S6. Experimental (red) and simulated (black) X–ray powder diffraction patterns of residues after TG analysis.

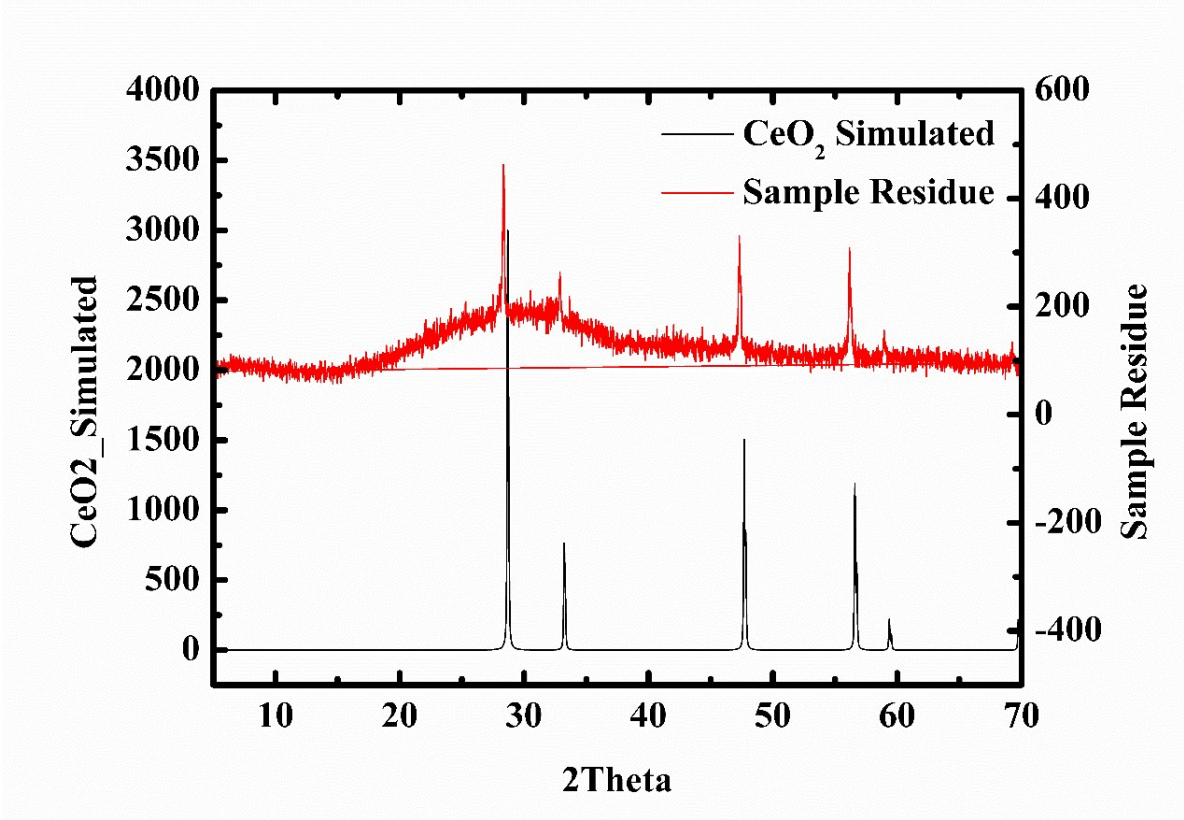

Figure S7. UV-vis-NIR diffuse reflectance spectra of $K_8Ce_2I_{18}O_{53}$.

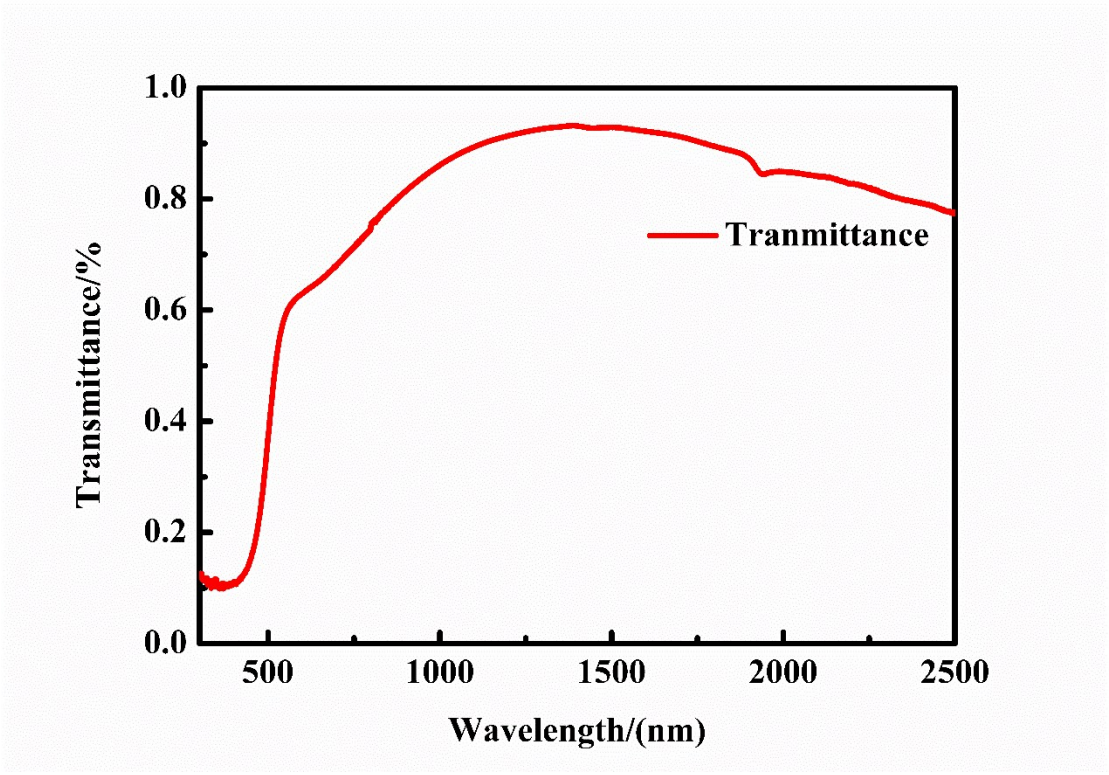

Figure S8. Different mechanism of RhB degradation in $K_8Ce_2I_{18}O_{53}$ and P25.

The hypsochromic shifts from 554 to 500 nm in RhB photodegradation clearly shows the different mechanistic pathways. As for $K_2Ce_8I_{18}O_{53}$, the N-deethylation process followed by the destruction of the skeleton, which account for the blue shift in the left diagram. On the contrary, P25 shows a totally different mechanism, which is a direct breakage of the aromatic ring caused by photosensitization process.